

Surface Plasmon Resonance Based Refractive Index Biosensor: A External Sensing Approach

Sumaiya Akhtar Mitu

MBSTU: Mawlana Bhashani Science and Technology University

Mst. Nargis Aktar

MBSTU: Mawlana Bhashani Science and Technology University

Sobhy Mohamed Ibrahim

King Saud University

Kawsar Ahmed (✉ kawsar.ict@mbstu.ac.bd)

Mawlana Bhashani Science and Technology University <https://orcid.org/0000-0002-4034-9819>

Research Article

Keywords: Surface plasmon resonance (SPR), Optical fiber sensors, Photonic crystal fiber (PCF), Plasmonic Material, High sensitivity

Posted Date: February 18th, 2022

DOI: <https://doi.org/10.21203/rs.3.rs-1329525/v1>

License: © ⓘ This work is licensed under a Creative Commons Attribution 4.0 International License.

[Read Full License](#)

1 Surface Plasmon Resonance Based Refractive Index Biosensor: A 2 External Sensing Approach

3 Sumaiya Akhtar Mitu¹, Mst. Nargis Aktar¹, Sobhy Mohamed Ibrahim², Kawsar
4 Ahmed^{1,3,*}

5 ¹Group of Bio-photomatiç, Department of Information and Communication Technology, Mawlana
6 Bhashani Science and Technology University, Santosh, Tangail-1902, Bangladesh

7 ²Department of Biochemistry, College of Science, King Saud University, P.O. Box: 2455, Riyadh 11451,
8 Saudi Arabia

9 ³Department of Electrical and Computer Engineering, University of Saskatchewan, 57 Campus Drive,
10 Saskatoon, SK S7N 5A9, Canada

11 *Corresponding Author: ORCID ID: 0000-0002-4034-9819

12 Emails: mitu.ict12@gmail.com, nargis.unsw@gmail.com, syakout@ksu.edu.sa, kawsar.ict@mbstu.ac.bd

13 **Abstract:**

14 A surface plasmon resonance (SPR) based sensor **founded on Photonic crystal fiber (PCF)** is
15 suggested and numerically analyzed in the manuscript. **The refractive index (RI) detecting SPR**
16 **based sensor has the ability to identify the analyte range from 1.33 to 1.4.** Pure silica is used as a
17 base material and it has high RI value than the analyte RI. Furthermore, an analyte layer and
18 chemically stable gold (Au) layer are also placed at the sensor design. The simulations are done
19 based on the Finite Element Method (FEM). Here, the scaled-down approach has the necessity to
20 increase phase **matching point within the core mode and surface plasmon polariton (SPP)** mode
21 which tends to the sensor to reach high sensitivity response. At the intersect point of core and
22 SPP mode, the loss curve shows a maximum peak value. **The suggested sensor shows the highest**
23 **wavelength sensitivity (WS) response of 35,943.22 nm/RIU, amplitude sensitivity (AS) response**
24 **of 2321.36 RIU⁻¹, sensor resolution of 9.04×10⁻⁶ RIU, and Figure of merit (FOM) value of 600.**
25 It is noted that all the optical parameters show better performance analysis. Furthermore, an
26 external sensing approach provides more fabrication feasibility **which marks the offered sensor**
27 **more suitable for practical experimentation. Besides, the investigated sensor provides the**
28 **maximum and rapid sensing performance that will be helpful for microfluidic analyte detection,**
29 **detection of biomolecules, medical diagnostics, virus detection, security, and bio-imaging.**

30 **Keyword:** Surface plasmon resonance (SPR); Optical fiber sensors; Photonic crystal fiber
31 (PCF); Plasmonic Material; High sensitivity.

32 **Introduction:**

33 In the 21st century, Photonic Crystal Fiber (PCF) forms a new way for the improvement of
34 Refractive Index (RI) based sensors. It is also known as micro-structured optical fibers or the
35 holey fibers [1]. Light is confined through the fundamental core of the PCF-based structure. The
36 characteristics and performances of the optical sensor can be extended through the use of various
37 liquids [2], metals [3], liquid crystal [4], or oil [5]. In the past decades, PCF based SPR sensor
38 was the most explored technique than the other structures such as modal interferometers [6],
39 Fiber Bragg grating (FBGs) [7], micro-ring resonator, multimode interference, long-period fiber
40 gratings (LPFGs) [8], and resonant mirror [9]. Besides, the non-PCF based SPR sensors were
41 also analyzed in [10, 11]. The SPR based sensor was introduced first both for bio sensing and
42 gas-detection in 1983 [12]. Basically, SPR is the combination of the PCF technology and
43 plasmonic science where gold (Au) is applied as a plasmonic material and the analyte is used as
44 an investigated liquid. In the SPR based technology, light conducts electrons between the
45 interface of the gold and analyte. Previously, prism and metal layer were used in the SPR based
46 sensor but due to some limitations, recently PCF based SPR technology has drawn attention for a
47 large number of advantages. This SPR sensor is able to overcome the limitations of bulky and
48 remote sensing features [13]. The noticeable features of SPR sensor are effectiveness [14], low
49 loss [15], real-time detection [16], broad mode area [17], and so on. Moreover, SPR based
50 sensing technique has a large number of applications on control food quality [18], environment
51 monitoring [19], gas detection, medical diagnostics [20], bio-molecular analyte detection,
52 security, virus detection [21], and bio-imaging [22].

53 Various analysis have been performed to design a sensor with high sensitivity response. To rise
54 the sensing performance as well as minimize the loss value is the main focus of the
55 investigations. From the previous analysis, the maximum wavelength sensitivity response of
56 5500nm/RIU was noted for a liquid-core PCF-based plasmonic sensor [23]. More investigations
57 were performed to improve the sensing performance in addition to reduce the loss value.
58 Additionally, Dash et al. [24] anticipated a Graphene based D Shaped PCF Biosensor and
59 obtained the sensing response of 3700 nm/RIU and the amplitude sensitivity response of 216
60 RIU⁻¹. Though the wavelength sensitivity (WS) response was lower than the previous analysis
61 but a new parameter of amplitude sensitivity response was indicated here. Later more
62 investigations were performed to increase the amplitude sensitivity (AS) response. Likewise,

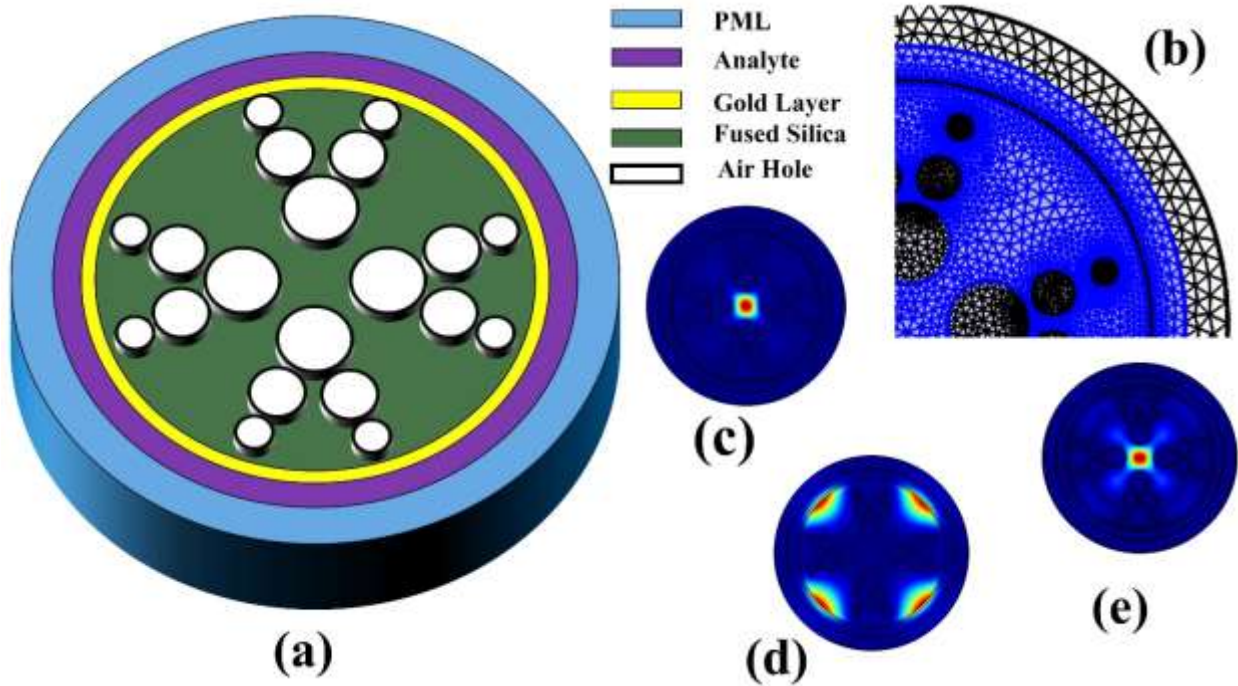
63 a Graphene-Based PCF sensor was demonstrated and shown the highest amplitude sensitivity
64 response of 860 RIU^{-1} and also reported the resolution as $4 \times 10^{-5} \text{ RIU}$ with the loss value of 160
65 dB/cm [13]. Moreover, dual-core D-shape PCF sensor was suggested to get the sensitivity and
66 resolution value of 14660 nm/RIU and $6.82 \times 10^{-6} \text{ RIU}$ respectively with the loss value of 80
67 dB/cm [25]. Furthermore, the WS and AS responses of $25,000 \text{ nm/RIU}$ and 1411 RIU^{-1} was
68 achieved with the highest Figure of merit (FOM) value of 502 for the analyte RI range from 1.33
69 to 1.38 [26]. In recent years, more researches have been performed on the design, materials, and
70 analytes to get high sensitivity responses. Recently, in the year 2020, a duplex core SPR sensor
71 has been intended and reported the AS response of 1770 RIU^{-1} for the analyte RI value from
72 1.33 to 1.40 and the WS response of $10,700 \text{ nm/RIU}$ is noted [27]. Additionally, the WS
73 response of 45003.05 nm/RIU has been achieved using a Au layer thickness of 50 nm [28]. The
74 reported sensitivity was better than the previous works but the gold layer thickness was very
75 high.

76 In this manuscript, an SPR based sensor structure is designed using an external sensing
77 mechanism. The suggested sensor is highly sensitive to detect the unknown analyte.
78 Additionally, scaling down air hole diameter controls the light-guiding mechanism [29].
79 Basically, scaling down air holes provide better propagation and light direction that is
80 responsible to increase the coupling between core and SPP mode. The offered sensor provides
81 maximum sensitivity response with a low loss value. The numerical investigates has been
82 performed based on the FEM method. The main goal of this investigation is to gain high WS and
83 AS with better resolution, and maximum value of FOM. The manufacture feasibility of the
84 suggested sensor will help to explore the opportunity for commercial utilization.

85 **Design and Methodology:**

86 The structural cross-sectional three dimensional vision of the proposed sensor is given in Fig.
87 1(a). The mesh analysis for the structural view is also shown in Fig. 1(b). There are 10126
88 domain elements in the entire mesh. The mode distribution fields are also exhibited in Figs 1 (c),
89 (d), and (e) for the core, SPP, and coupling modes respectively. The numerical examinations of
90 the simulated sensor are carried out using the commercially available COMSOL Multiphysics
91 (version 5.5). The FEM is used for further investigations which makes the boundary conditions
92 and perfect match layer (PML) are also used to reduce the scattering of light. The structural
93 parameters of the design are chosen through the variations of the value of parameters. Finally,

94 three layers and different sizes of air holes are selected with diameters of 1.6 μm , 1.2 μm , and
 95 0.8 μm respectively. The thickness of the layers of gold and analyte are taken at 20 nm and 0.7
 96 μm respectively. The PML layer of the proposed sensor has been used as 1 μm . Typically, the
 97 PML layer is used to fascinate the scattering of light.
 98

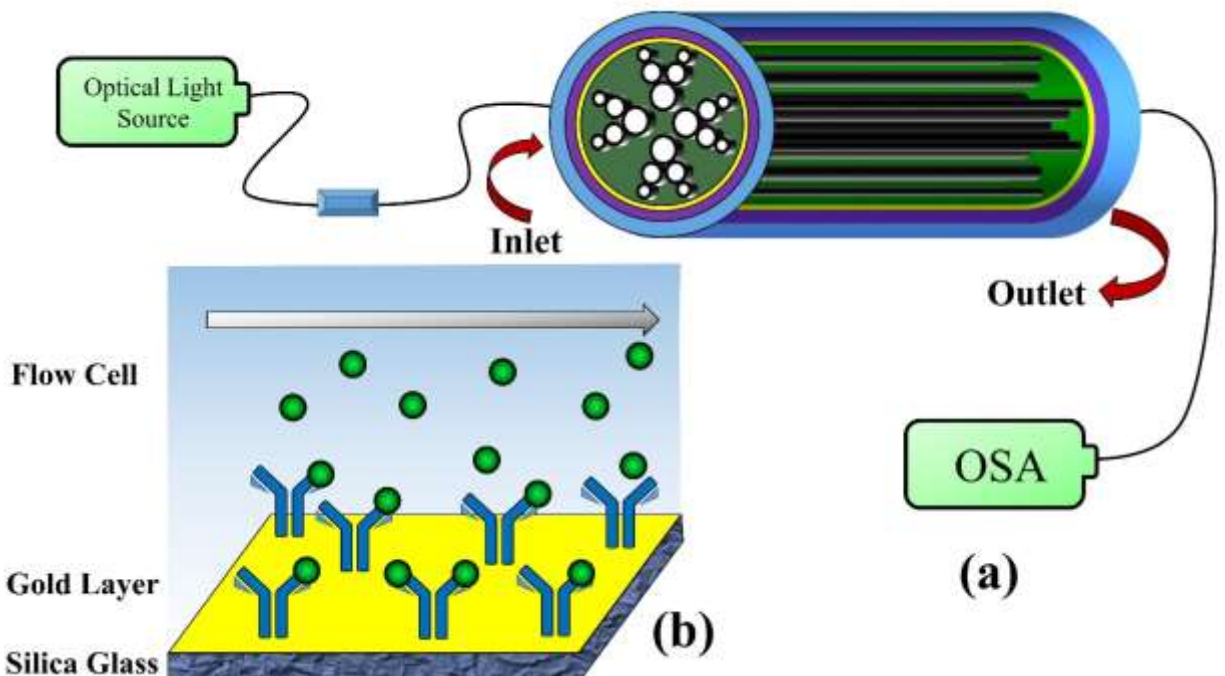


99
 100 Fig. 1. The physical design analysis of the investigated sensor, (a) for simulated structure design,
 101 (b) mesh analysis of the suggested sensor, (c) Fundamental or the core mode, (d) SPP mode, and
 102 (e) coupling mode field distributions.

103 The PML layer of the structure is marked by blue color in Fig. 1 (a). Besides, the fundamental
 104 core mode propagates light at the core region, the SPP mode creates plasmon at the interface
 105 between the gold layer and analyte layer and the coupling mode indicates the more scattering of
 106 light from core mode to the SPP mode. This coupling or phase matching occurs at the point of
 107 highest peak loss. All these mode distributions are highlighted into the sub figures of Fig. 1(c).
 108 (d) and (e).

109 Although the investigation is simulation-based, the generalized schematic block diagram of the
 110 experimental operation of the suggested sensor is exhibited in Fig. 2(a). A light source
 111 (broadband or monochromatic) can carry the optical power into single-mode fiber (SMF). The
 112 connection between the light and PCF can be established through upper standard SMF. On the

113 other hand, lower standard SMF can connect PCF and optical spectrum analyzer (OSA).
 114 Furthermore, OSA or photo-detector can easily detect the transferred light. Moreover, a
 115 computer display has been used to observe the outputs. The Inlet and outlet section can control
 116 the flow or change of the analyte through withdrawal or pumping process. The movement flow
 117 of the free electrons of the sensor within the interface of the gold layer and analyte has been
 118 drawn in Fig. 2(b).



119 Fig. 2. (a) Schematic block diagram for experimental setup, and (b) Movements of free electrons
 120 at the interface between Au and analyte layer.
 121

122 The oscillations of the free electrons become started at the interface of the Au and analyte layer
 123 when the light hits the gold layer. When the light is supplied from the optical light source then
 124 the light is transmitted through the fiber sensor and creates different modes as core and SPP. At a
 125 point of high loss value, coupling mode is obtained. These modes are corresponding output
 126 figures can be achieved through Optical Source Analyzer.

127 **Fabrication:**

128 The fabrication technique of the sensors can be two types, internal and external sensing
 129 techniques [30]. In the internal detecting approach, the internal air holes are covered with
 130 plasmonic materials and analytes [31]. As a result, the fabrication process is difficult as liquid
 131 intrusion and selective metal covering are required. Recently, external sensing is an attractive

132 approach and preferred much for the fabrication feasibility [32]. In this type of sensing, the
 133 plasmonic material coating and analyte layer are kept outside of the PCF sensor. The external
 134 sensing approach is better to compare to internal sensing for real-time applications. As the layer
 135 thickness, layer deposition, and analyte filling can easily be controlled through this technique.
 136 Additionally, the circular air holes can be easily fabricated through capillary stacking, and stack-
 137 and-draw processes [33].

138

139 Numerical Analysis:

140 In the proposed investigation, silica or silicon dioxide (SiO₂) is used as both ground material and
 141 PML layer. The air holes are arranged in three different layers within the silica. The RI value of
 142 SiO₂ is changed with the variations of the operating wavelength. All the equations are analyzed
 143 for the temperature 20 °C. The analytes of lower RI can easily be sensed by using silica.
 144 Sellmeier Equation (1) is used to measure the dispersion values of silica.

145

$$146 \quad n_{silica}(\lambda) = \sqrt{1 + \sum_{i=1}^j \frac{A_i \lambda^2}{\lambda^2 - B_i^2}} \quad (1)$$

147 where, λ (μm) denotes the wavelength and the constant values of the Sellmeier coefficients can
 148 be represented by A_i and B_i . These fixed values of A_1 , A_2 , A_3 , B_1 , B_2 , and B_3 are 0.696750,
 149 0.408218, 0.890815, 0.069066, 0.115662, and 9.900559 respectively [34].

150 At the time of light propagation within the core region, free electrons start moving through the
 151 plasmonic material. As a result, an oscillation is generated at the interface of the plasmonic
 152 material and the metal-dielectric. Mainly, the execution of the SPR sensor depends on the
 153 plasmonic material. Normally, Au, copper (Cu), silver (Ag), Aluminum (Al) are used as a
 154 plasmonic material in the sensors [35]. Among them, though silver offers a better resonance
 155 peak, it is a chemically unstable material [36]. To overcome this problem of oxidization gold can
 156 be used as it is reliable and chemically stable material than all other materials [37]. This is the
 157 main reason to select a tiny gold layer for this analysis. The RI of gold can be chosen from
 158 Drude–Lorenz Equation (2).

$$159 \quad \varepsilon_{Au} = \varepsilon_{\infty} - \frac{\omega_D^2}{\omega(\omega + j\gamma_D)} + \frac{\Delta\varepsilon \cdot \Omega_L^2}{(\omega^2 - \Omega_L^2) + j\Gamma_L \omega} \quad (2)$$

160

161 where, ϵ_{Au} refers to the gold permittivity. The constant coefficient values are chosen from Rakić
 162 *et al.*, (1998). Moreover, FEM is used to numerically simulate the planned SPR based sensor
 163 design. In addition, a wide range of wavelength is analyzed for the suggested sensor.
 164 Therefore, the loss spectrum of the core mode can be measured from the unreal part of the
 165 effective RI values using Eq. (3) [38]. Based on the loss curve the effectiveness of the sensor has
 166 been realized.

$$167 \quad \alpha_{Loss}(dB/cm) = 8.686 \times k_0 \text{Im}g(n_{eff}) \times 10^4 \quad (3)$$

168 Here, k_0 refers to the free space wave number whose value is $k_0 = 2\pi/\lambda$, $\text{Im}g(n_{eff})$ defines the
 169 unreal part of the effective RI and λ is the operating wavelength.

170 The AS response can be evaluated from the loss peak of the anticipated sensor. It is also known
 171 as cost-effective method. This parameter can be measured using the amplitude interrogation
 172 method following Eq. (4) [39]

$$173 \quad S_A(RIU^{-1}) = -\frac{1}{\alpha(\lambda, n_a)} \cdot \frac{\delta\alpha(\lambda, n_a)}{\delta n_a} \quad (4)$$

174 where $\alpha(\lambda, n_a)$ indicates the overall loss value for the effective RI is equal to n_a , $\delta\alpha(\lambda, n_a)$
 175 represents the change of two consecutive loss peaks for the variations of the analyte RI, and δn_a
 176 refers to the change of RI values.

177 Besides, the wavelength sensitivity (WS) response is a vital parameter for the performance
 178 analysis of a sensor. Usually, the wavelength interrogation method displays maximum sensing
 179 performance from the amplitude interrogation method [40]. The WS response of the simulated
 180 structure can be determined by using Eq. (5) [40]

$$181 \quad S_\lambda(nm/RIU) = \frac{\Delta\lambda_{peak}}{\Delta n_a} \quad (5)$$

182 where, $\Delta\lambda_{peak}$ and Δn_a denotes the alteration between the resonance peaks and the analyte RI
 183 respectively.

184 Sensor resolution is also another parameter to evaluate sensor performance. It controls the degree
 185 of dielectric RI detection. This parameter can be calculated by Eq. (6) [41]

$$186 \quad R(RIU^{-1}) = \Delta n_a \Delta\lambda_{min} / \Delta\lambda_{peak} \quad (6)$$

187 Where, Δn_a refers to the difference of analyte RI, λ_{min} indicates the minimum peak
 188 wavelength and $\Delta\lambda_{peak}$ specifies the difference of the peak wavelengths.

189

190 Figure of merit (FOM) can be evaluated from the value of WS or AS. The FOM can be
 191 calculated by Eq. (7) [42],

$$192 \quad FOM = \frac{S_\lambda}{FWHM} \quad (7)$$

193 where S_λ mentions the value of WS. Therefore, FWHM specifies the full width of half maximum
 194 peak resonance. The parameters of this investigation are summarized in Table. 1. All the
 195 parameters are upheld here to visualize at a glance.

196 Table. 1. Symbols of all parameters with explanations those are used in this simulation.
 197

SI No	Symbol	Description
1	n_{silica}	RI of silica
2	λ	Operating wavelength
3	ϵ_{Au}	Gold permittivity
4	α_{Loss}	Confinement loss
5	n_a	Analyte RI
6	S_A	Amplitude sensitivity
7	S_λ	Wavelength sensitivity
8	R	Resolution
9	FWHM	Full Width Half Maximum
10	FOM	Figure of Merit

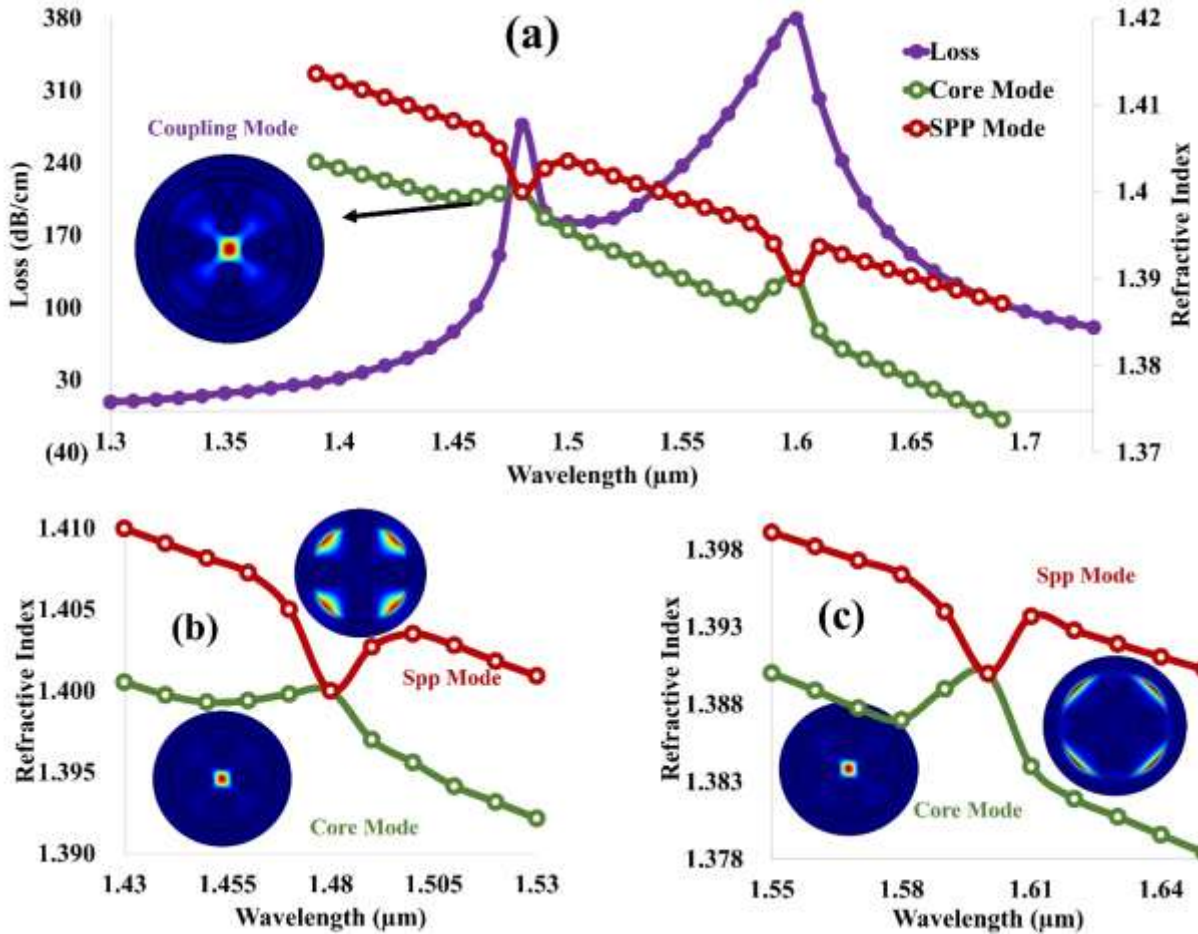
198

199 Results and Discussion:

200 In the SPR based mechanism, the RI (real value) of the fundamental and SPP mode transect at a
 201 particular point where the operating wavelength gets a loss intense peak. This occurrence is
 202 recognized as the phase-matching condition [43]. In Fig. 3, the dispersion relation is upheld for
 203 the analyte RI 1.33 where two intersect points have been gained for the proposed sensor. The real
 204 value of core and SPP mode intersects at the wavelength of 1.48 μm and 1.6 μm . In the phase-
 205 matching points or intersect points, extreme energy is moved from the fundamental core mode to
 206 SPP mode.

207

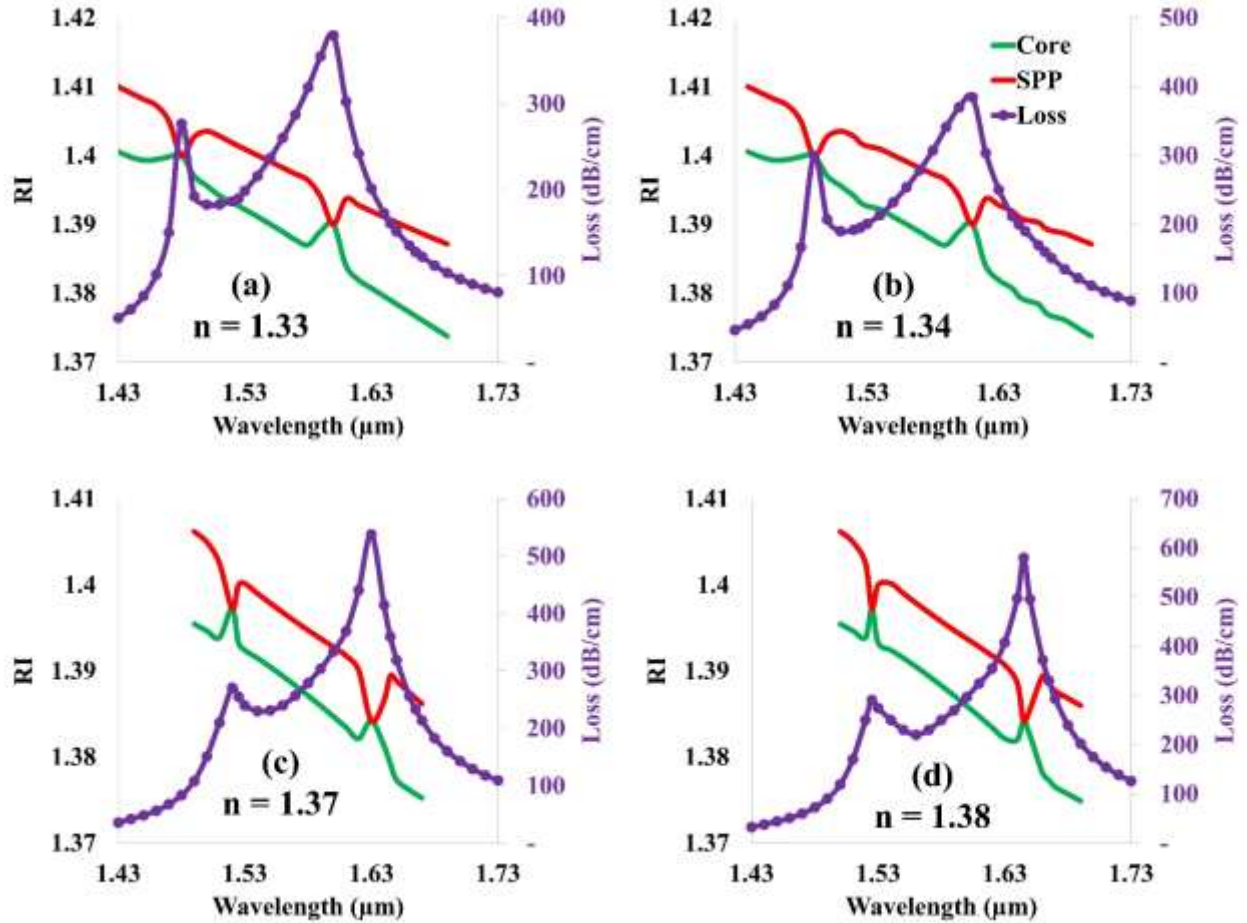
208



209
 210 Fig. 3. (a) Wavelength dependent dispersion relation of core and SPP mode with loss value, (b)
 211 first intersect point, (c) second intersect point.
 212

213 The dispersion relations for the different analytes are also exposed in Fig. 4. It is realized that the
 214 intersect points are growing with the variations of analyte RI. The first intersect points are found
 215 at the operating wavelength at 1.48 μm, 1.49 μm, 1.52 μm and 1.525 μm and the second intersect
 216 points are gained at the operating wavelength 1.6 μm, 1.61 μm, 1.63 μm and 1.645 μm for the
 217 analyte 1.33, 1.34, 1.37 and 1.38 respectively. Due to the variations of analyte RI, the phase
 218 matching wavelengths are indicated through red and green line for the respective core and SPP
 219 modes.

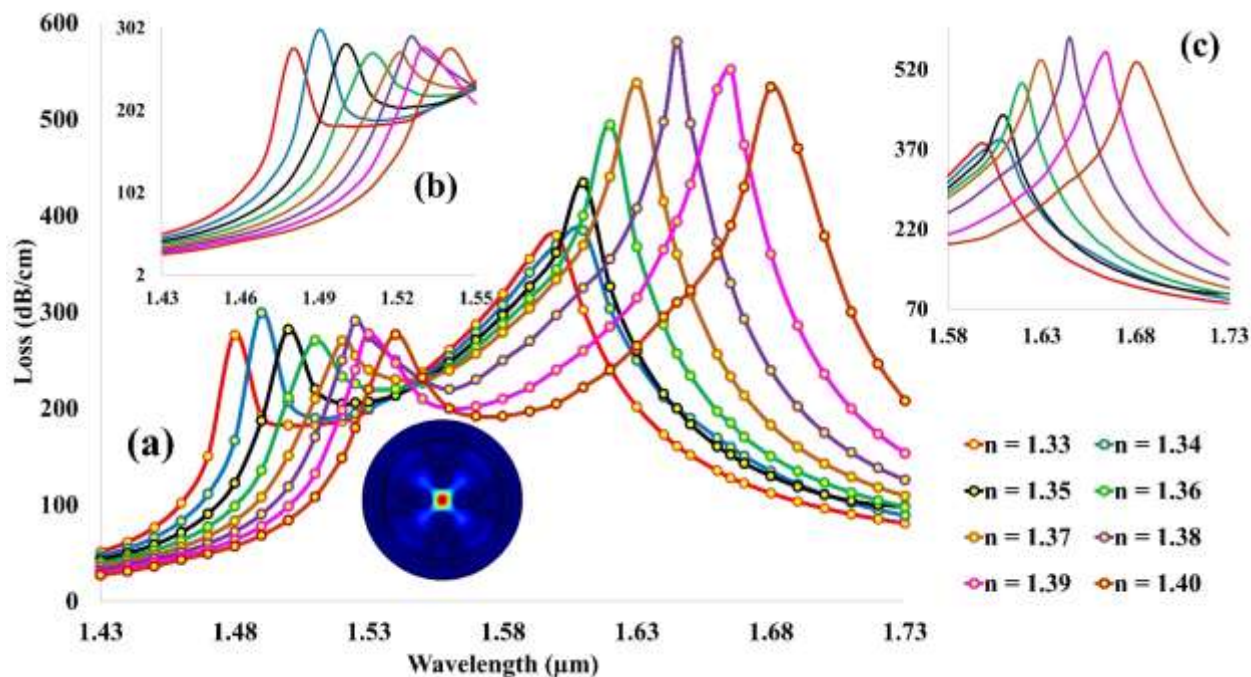
220



221
 222 Fig. 4. Wavelength dependent dispersion relation of fundamental and SPP mode with loss value
 223 for the variations of different analytes.

224
 225 At the phase-matching points the loss value shows the maximum peak value. The confinement
 226 loss values for the offered sensor are exhibited in Fig. 5 for the variants of the analyte RI within
 227 1.33 to 1.4 where two-loss peak points have been achieved. Moreover, the second peak shows a
 228 higher value than the first peak. Different color lines have been used to clearly identify the loss
 229 values for each analytic RI. It is noticed that the highest loss value is obtained for the analyte
 230 1.38 at the wavelength of 1.645 μm. At that point, the maximum loss value of 580.34 dB/cm is
 231 attained. Besides, the zoom portion of the first peak and second peak are also displayed in Fig. 5
 232 (b) and (c). The loss peak points gradually shift with the variation of analyte. The low loss value
 233 is gained for the analyte 1.33. So that it is cleared that the loss values are increasing with regard
 234 to the rise of analyte RI. The low loss value of 27 dB/cm and the extreme peak loss value of 277
 235 dB/cm are reached for the proposed sensor design. Basically, the low loss values define the

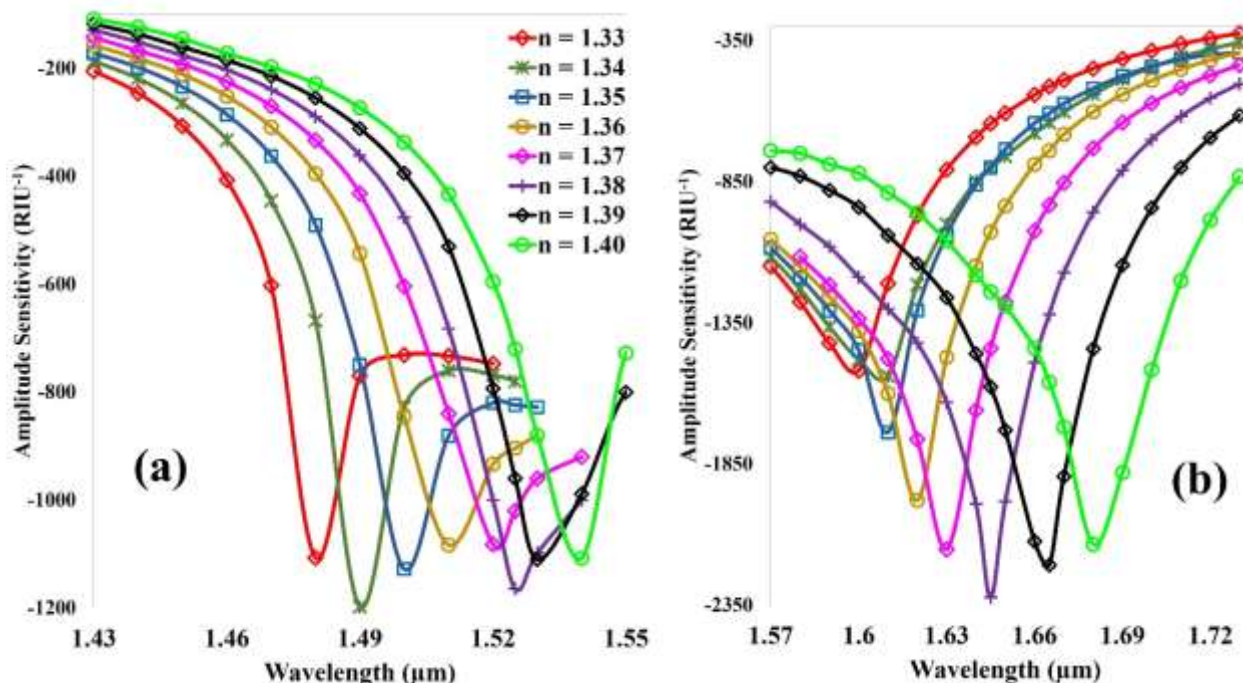
236 sensor effectiveness as well as scattering. The low-loss sensor is most suitable for practical
 237 implementation. Based on these peak loss values another important parameter named amplitude
 238 sensitivity can be easily derived.
 239



240
 241 Fig. 5. Confinement loss spectrum with regard to the wavelength change for the variations of
 242 analyte from 1.33 to 1.4.
 243

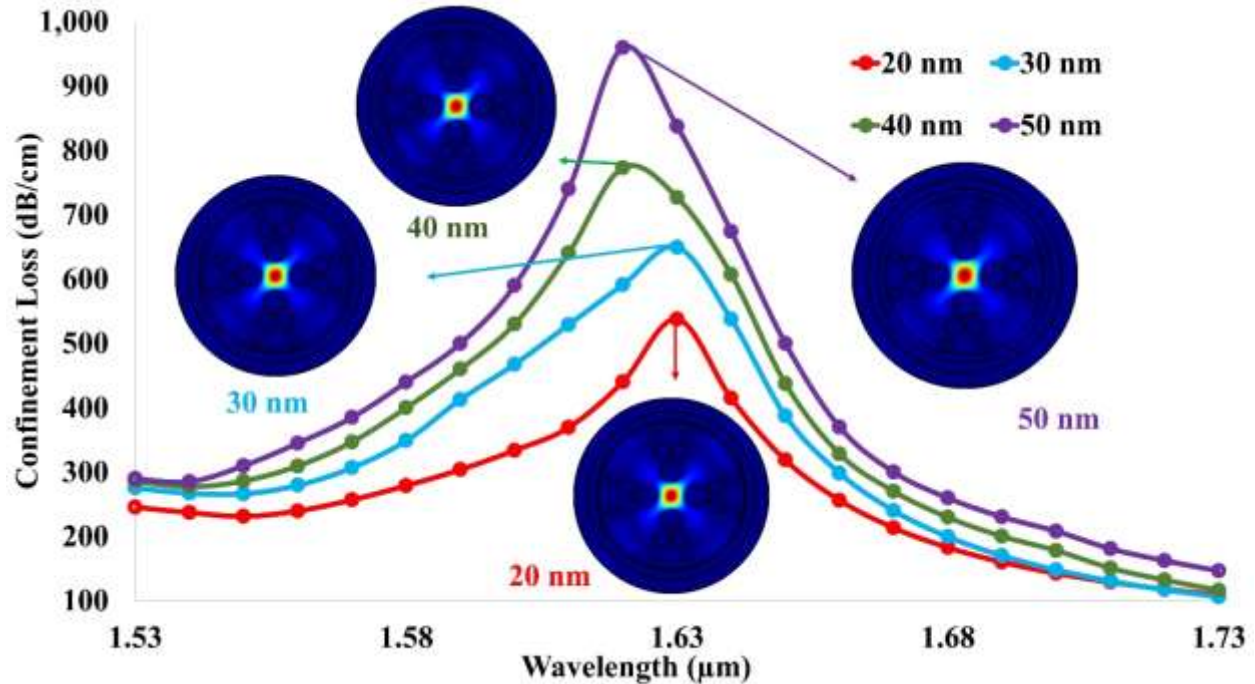
244 The AS is also a vital parameter for the measurement of sensor efficiency. The values of the AS
 245 mostly depend on the peak values of the confinement losses. To gain the high AS response, the
 246 offered structure has been reshaped and resized. The corresponding AS response for the
 247 suggested sensor scheme is given in Fig. 6. The AS response for the two-loss peaks are revealed
 248 in Figs 6 (a) and (b). The first part of the amplitude sensitivity response is downward up to the
 249 peak point. After reaching the peak point, the graphs again show upward characteristics. The
 250 maximum AS response of $-2321.36 \text{ RIU}^{-1}$ is attained for the design at the wavelength of 1.645
 251 μm for the RI 1.38. Besides, in the first peak value the maximum AS is noted as $-1197.57 \text{ RIU}^{-1}$
 252 for the analyte 1.34. Comparing two of these values the maximum response is noticed for the RI
 253 1.38. Based on this AS response the sensor's compactness can also be determined. So, from the
 254 confinement loss analysis and AS response investigation, the maximum performance analyte is

255 selected as 1.38. Now, it is also an important task to analyze the performance according to the
 256 gold layer variations.



257
 258 Fig. 6. Amplitude sensitivity response with respect to the wavelength change for the variations of
 259 analyte from 1.33 to 1.4. (a) for 1st peak and (b) for 2nd peak.

260
 261 The conforming loss spectrum for the variations of the Au layer is exhibited in Fig. 7 with the
 262 corresponding mode field distributions. The four colored lines of red, blue, green, and violet are
 263 used to indicate the four gold layer thicknesses. The extreme loss peak of 960 dB/cm is gained
 264 for the Au layer wideness of 50 nm at the operating wavelength of 1.62 μm. Moreover, a low
 265 loss value is obtained for the thickness of 20 nm at the operating wavelength of 1.63 μm. The
 266 loss curve is increasing with the rise of Au thickness. As the Au layer is costly, so based on this
 267 problem and loss curve analysis 20 nm thickness is picked for the sensor design.



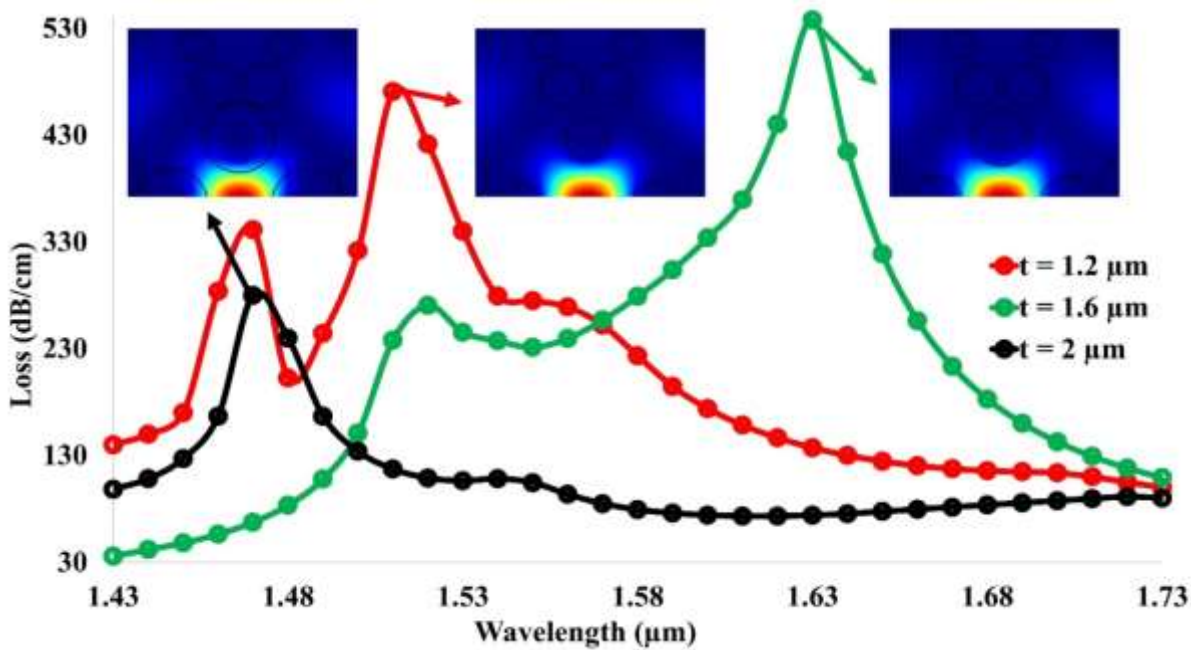
268 Fig. 7. Loss spectrum with respect to the variations of gold layer from 20 nm to 50 nm.
 269

270 Gold layer thickness is varied from 20 nm to 40 nm. As, much amount of gold is responsible to
 271 costly fiber. In the contrary, little amount of gold can't give better outcomes. For this reason, the
 272 thickness of 20 nm is chosen for this investigation.

273
 274 Moreover, the air hole diameter is also changed for further investigations. Among the three-layer
 275 air holes, the innermost air holes of the design are tuned and the obtained results are shown in
 276 Fig. 8. In the meantime, the diameters of the smaller air holes are also changed but the results do
 277 not affect any more by these variations. As a result, the outcomes of the smaller air holes
 278 diameter changes are not highlighted here. The variations of the larger air hole diameters affect
 279 the loss value highly. From the graphical observation, it is pointed that two sharp loss peaks are
 280 gained for the diameter of 1.6 μm. The diameter value is changed from 1.2 μm to 2 μm. It is
 281 investigated that the light scattering is high for the diameter of 2 μm. As well as the diameter of
 282 1.2 μm also responsible for scattering some light from the core to the gold layer. From this
 283 analysis, the air hole diameter of 1.6 μm is chosen for performing more operations.

284 The corresponding AS responses for the air hole diameter variations are upheld in Fig. 9. Three
 285 peaks are found for the three values. Among them the maximum response of $-2151.39 \text{ RIU}^{-1}$ is
 286 gained for air hole diameter of 1.6 μm at the wavelength of 1.63 μm. The lowest peak is attained

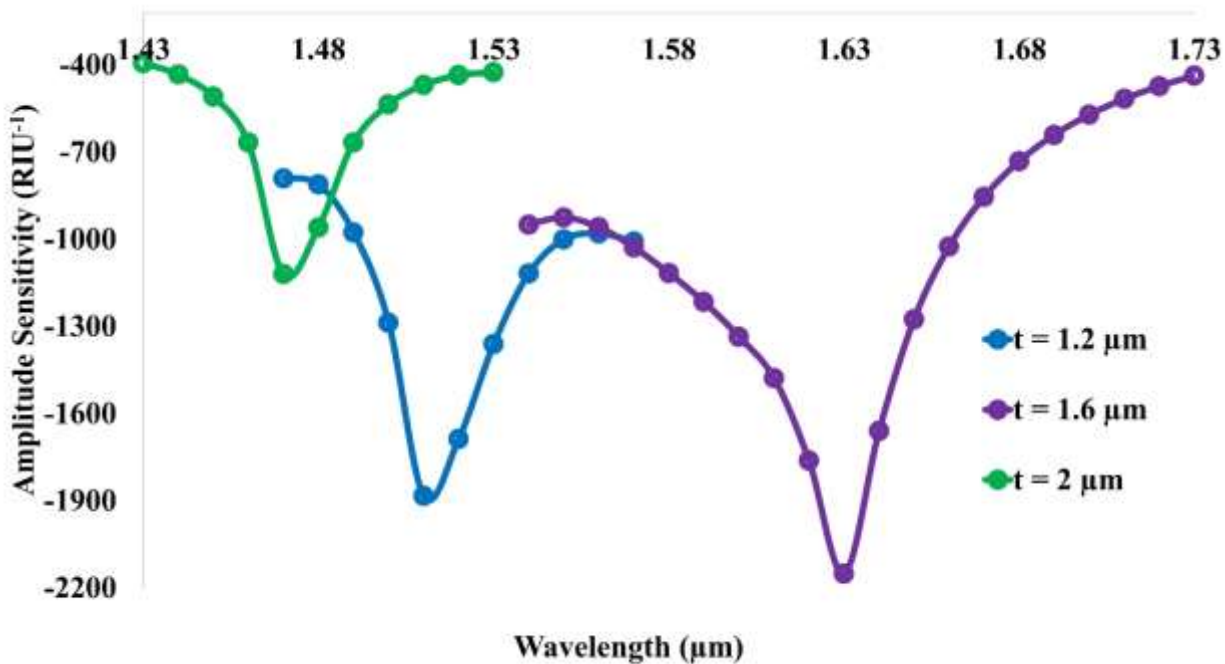
287 for the diameter of 2 μm at the operating wavelength of 1.47 μm . Additionally, the middle
 288 average value of $-1883.52 \text{ RIU}^{-1}$ is achieved for the air hole diameter of 1.2 μm at the
 289 wavelength of 1.51 μm .



290

291

Fig. 8. Confinement loss spectrum for the variations of air hole diameter.



292

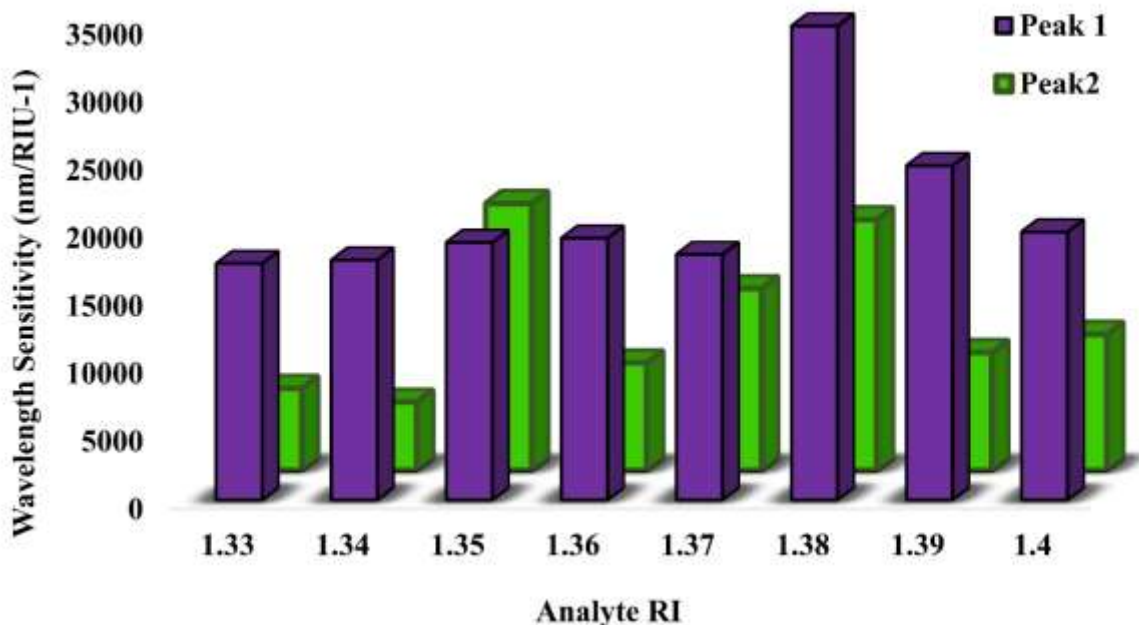
293

294

Fig. 9. Amplitude Sensitivity response for the variations of air hole diameter.

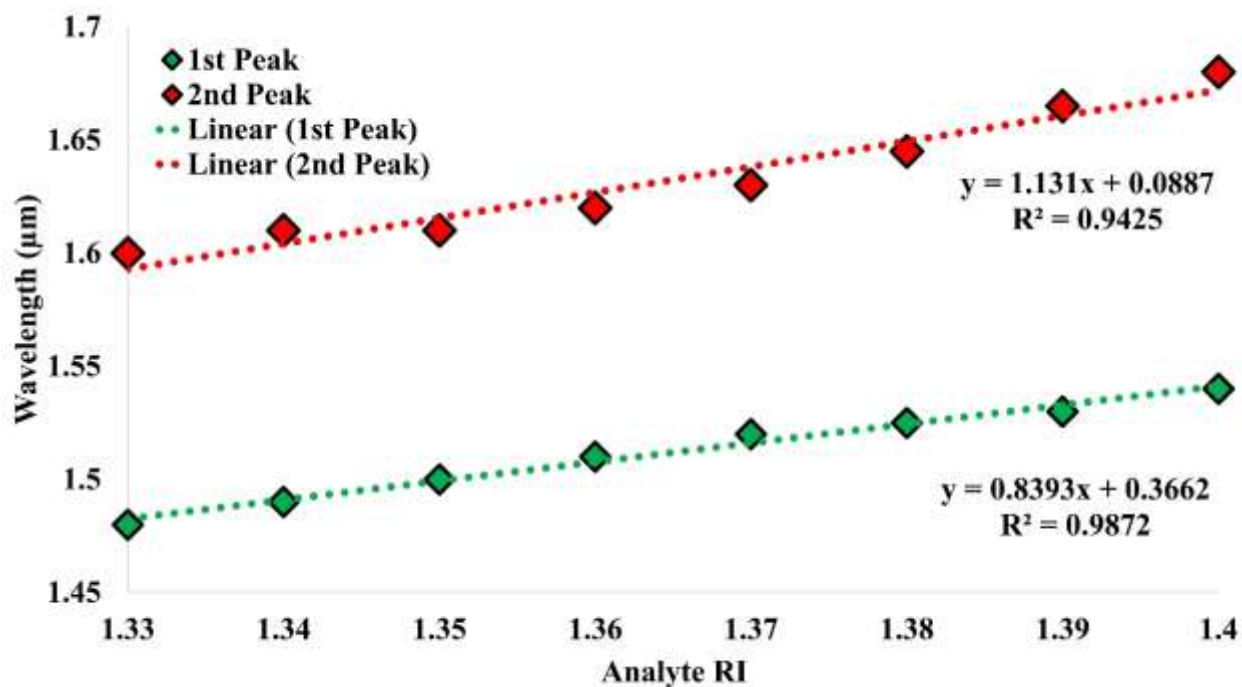
295 Another significant parameter is Wavelength Sensitivity (WS) response. Based on this parameter
 296 the effectiveness and the overall performance can be analyzed. As there is a noticeable value of
 297 WS is achieved, so it can be claimed that the proposed sensor will fit for practical use by
 298 reducing fabrication complexity with high sensitivity response. In Fig. 10, two bar graphs are
 299 displayed where the blue graph indicates the values for the first peak value and the green bar
 300 graph defines the values for the second peak values. For the analyte 1.33 to 1.4. The first loss
 301 peak values have given lower peak values than the second peak. Otherwise, the WS responses
 302 are higher for the first peak than the second peak value. Moreover, the maximum WS response of
 303 35943.22 nm/RIU is attained for the RI 1.38 and the second-highest value of 25646.58 nm/RIU
 304 is reached for the RI 1.39. Both WS response values are noted for the second peak values. This
 305 high sensitivity response will help the structure suitable for more accurate sensing performance.
 306 From Fig. 10, it can be said that the WS response is gradually growing from analyte 1.33 to 1.38.
 307 On the other hand, after reaching the highest sensitivity response it is started to decrease.
 308 Similarly, in the second peak, it is seen that WS is increasing and after reaching a particular point
 309 the value is decreasing again.

310



311 Fig. 10. Wavelength Sensitivity response for the differences of RI from 1.33 to 1.4 for two peak
 312 values.
 313

314 Based on the loss spectrum and sensitivity analysis, the dip wavelength for the simulated
 315 structure is cleared in Fig. 11. The resonance wavelengths for the variations of analyte 1.33 to
 316 1.4 are observed here. The polynomial fitting responses for the analyte RI changes are analyzed
 317 where the fitting response with for first peak value and with for second peak value. The
 318 polynomial fitting response is indicated by red and green markers. Besides, the linear fit curve is
 319 also drawn using red and green dash lines to determine the similarity between them.
 320



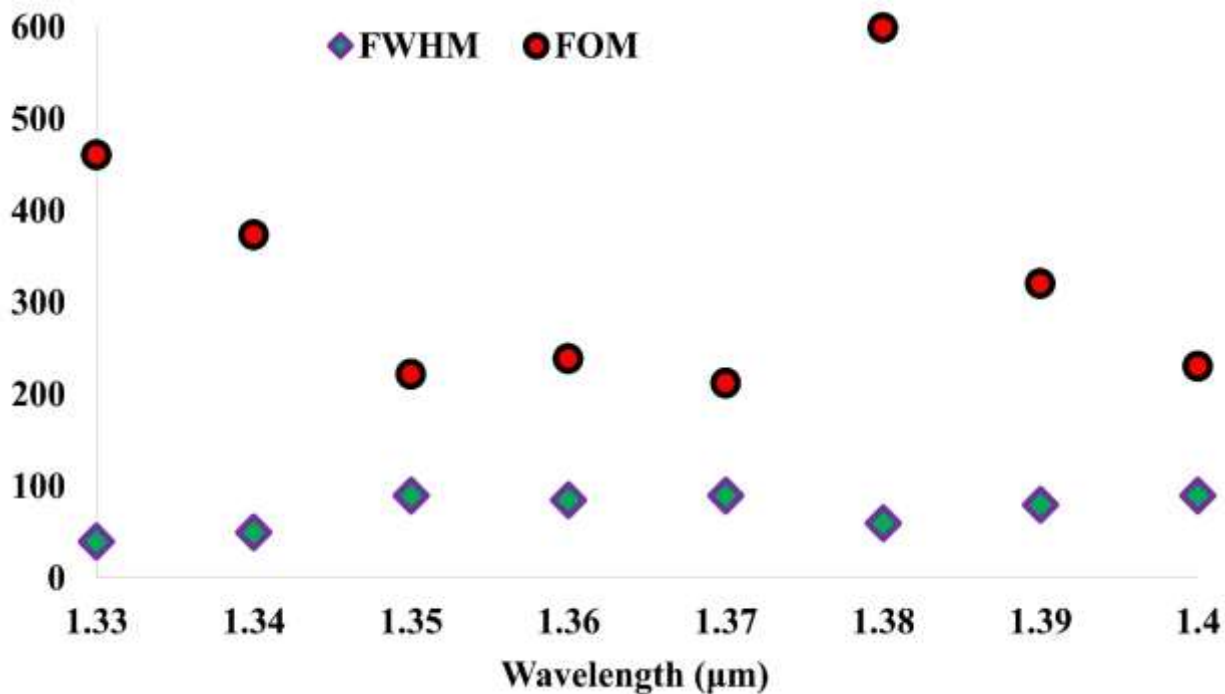
321 Fig. 11. Resonance wavelength with the variations of analyte RI from $1.33 \leq n_a \leq 1.4$ with
 322 fitting responses.
 323
 324

325 The Resolution of a sensor specifies the smallest RI changes detection capability. It can be
 326 calculated through the peak wavelength differences. The suggested sensor resolution of $9.04 \times$
 327 10^{-6} RIU for the analyte 1.40 is obtained by considering the gold layer wideness of 20 nm. As a
 328 result, the offered sensor is adept to detect 10^{-6} order of the RI change.

329 The Figure of Merit (FOM) specifies the overall quality of a device. Usually, the high value of
 330 FOM indicates high performance. The high value of FOM depends on high sensing performance
 331 and low full width half maximum (FWHM) value. FOM becomes high when the sensitivity
 332 response shows the highest value. In the proposed work, the FWHM value is decreasing

333 significantly as well as the sensitivity response is increasing. As FOM can be measured through
 334 the sensitivity response and FWHM, so the proposed sensor shows the maximum FOM value of
 335 600 for the RI 1.38 with the FWHM value of 60. On the contrary, the minimum value of FOM of
 336 212 is gained for the analyte 1.37. The respective FWHM and FOM are presented in Fig. 12
 337 where diamond shape markers are used to clarify the value of FWHM and circular shape markers
 338 are used to indicate the value of FOM.

339



340

341 Fig. 12. Full Width Half Maximum (FWHM) and Figure of Merit (FOM) variations.

342

343 At that moment, the overall simulation analysis of the designed sensor design are summarized in
 344 Table 2. A large number of parameters have been observed for the effectiveness and quality
 345 measurement of the sensor. From Table 2, it is noticeable that good outcomes have been
 346 achieved for the respective sensor design. Owing to a low confinement loss peak of 299.39
 347 dB/cm, the maximum values of wavelength sensitivity, amplitude sensitivity, resolution and
 348 FOM values are 35,943.22 nm/RIU, 2321.36 RIU⁻¹, 9.04×10^{-6} RIU and 600 respectively have
 349 been gained. These high values of the sensor will make the simulated structure more operative.

350

351

352 **Table. 2: Overall performance examination of the proposed sensor's sensing parameters.**

353

Analyte RI	PW(nm)		PL(dB/cm)		WS (nm /RIU ⁻¹)	AS (RIU ⁻¹)	Resolution (RIU ⁻¹) (×10 ⁻⁶)	FWHM	FOM
	Peak1	Peak2	Peak1	Peak2					
1.33	1480	1600	276.66	379.65	18429.38	1518.61	8.05	40	461
1.34	1490	1610	299.39	384.67	18681.18	1538.69	7.89	50	374
1.35	1500	1610	281.96	434.43	19982.90	1737.72	7.15	90	222
1.36	1510	1620	270.83	494.45	20295.24	1977.79	7	85	239
1.37	1520	1630	270.54	537.85	19100.13	2151.39	7.63	90	212
1.38	1525	1645	291.08	580.34	35943.22	2321.36	3.34	60	600
1.39	1530	1665	277.51	551.91	25646.58	2207.64	5.09	80	321
1.40	1540	1680	276.85	533.48	20758.48	2133.91	9.04	90	231

354

355 From Table 3, it is clearly visible that the offered structure shows an improved performance
 356 compare to the existing sensors. Based on the operating wavelength the variations of analytes
 357 from 1.33 to 1.4, the FOM reaches 600 value that is much more than the previously noted values.
 358 In addition, the wavelength and amplitude sensitivities also indicate a good improvement parallel
 359 to the prior works. Although the resolution value is not as high as found in the previous analysis,
 360 this response is good enough for the detection capability. **Based on these good outcomes, the**
 361 **designed sensor can be used in the field of sensing for the detection of different analytes [44, 45].**

362 **Table. 3: Performance analysis of the proposed sensor in comparison to previous works.**

363

Analyte RI	Wavelength Sensitivity (nm/RIU ⁻¹)	Resolution (RIU ⁻¹)	Amplitude Sensitivity (RIU ⁻¹)	FOM	Ref.
1.33-1.38	4,600	2.17×10 ⁻⁵	420.4	----	[46]
1.33-1.42	11,000	9.1×10 ⁻⁶	1,420	407	[47]
1.40-1.43	15,180	5.68×10 ⁻⁶	---		[48]
1.40-1.44	9,600	1.04×10 ⁻⁵	1739.26		[49]

1.33-1.38	10,493	9.53×10^{-6}			[50]
1.20-1.40	3,751.5	1×10^{-5}			[51]
1.33-1.39	30,000	3.33×10^{-6}	1,212	508	[24]
1.18-1.36	20,000	5×10^{-6}	1054		[25]
1.33-1.37	5,000	4×10^{-5}	860	47	[13]
1.33-1.38	25,000	4×10^{-6}	1411	502	[26]
1.33-1.40	10,700	9.34×10^{-6}	1770		[27]
1.32-1.32	13,750	7.2×10^{-6}	400		[12]
1.46-1.48	10,800	1.95×10^{-5}	514		[13]
1.33-1.40	12,000	8.33×10^{-6}			[52]
1.36-1.41	8,000	1.25×10^{-5}	1560	266	[15]
1.33-1.40	35,943.22	9.04×10^{-6}	2321.36	600	This work

364

365 **Conclusion:**

366

367 The FEM method is used to construct and investigate an SPR-based multi-layer sensor with an
368 external sensing mechanism. Several parameters of the sensor are optimized to get better sensing
369 outcomes. The simulated structure attains maximum WS and AS response of 35,943.22 nm/RIU,
370 and 2321.36 RIU⁻¹. Besides, a large FOM value of 600 is obtained. Moreover, the sensor has
371 scaled small analyte variation detection capability. Gold is used as a plasmonic material that has
372 major impact on sensing by creating a phase-matching phenomenon. When the RI values of two
373 core and SPP modes cross, the phase-matching point can be obtained at that point. In this
374 wavelength, the loss value reaches the high peak value. A maximum peak loss value of 580.34
375 dB/cm is noticed for the operating wavelength of 1.63 μm. The examined structure can sense a
376 wide range of RI from $1.33 \leq n_a \leq 1.4$. Due to the favorable features such as high WS and AS
377 sensitivity responses and high value of FOM, the sensor will be helpful for practical use in
378 sensing. Furthermore, the investigated sensor can be the prospective candidate for a large
379 number of applications such as chemicals detection, gas detection, medical diagnostics, security,
380 virus detection, and bio-imaging.

381 **Funding:** This work was supported by Researchers Supporting Project number (RSP-2021/100),

382 King Saud University, Riyadh, Saudi Arabia.

383 **Acknowledgments:** The authors are also grateful to the Ministry of ICT, Peoples Republic of
384 Bangladesh for their support in Research.

385 **Conflict of Interest:** No competing interests.

386 **Declarations:**

387 **Availability of data and material:** Corresponding author on reasonable request.

388 **Code availability** Not Applicable.

389 **Authors' contributions** Conceptualization, K. Ahmed; data curation, formal analysis,
390 investigation, methodology, S.A. Mitu; funding acquisition, S.M. Ibrahim; project
391 administration, M.N. Aktar, K. Ahmed; resources, software, S.A. Mitu; supervision, M.N.
392 Aktar, K. Ahmed; validation, K. Ahmed; visualization, S.A. Mitu; writing—original draft, S.A.
393 Mitu, M.N. Aktar, S.M. Ibrahim, K. Ahmed; writing—review editing, S.A. Mitu, M.N. Aktar,
394 S.M. Ibrahim, K Ahmed.

395 **Ethics approval:** Not Applicable.

396 **Consent to participate:** Not Applicable.

397 **Consent for publication:** Not Applicable.

398 **Recourses:** COMSOL Multiphysics software (version 5.5) could be downloaded from for here:
399 <https://www.comsol.com/comsol-multiphysics>

400 **References:**

401 [1] Russell, P.S.J., 2006. Photonic-crystal fibers. *Journal of lightwave technology*, 24(12),
402 pp.4729-4749.

403 [2] Wang, Y., Yang, M., Wang, D.N. and Liao, C.R., 2011. Selectively infiltrated photonic
404 crystal fiber with ultrahigh temperature sensitivity. *IEEE Photonics Technology Letters*,
405 23(20), pp.1520-1522.

406 [3] Zhang, S., Yu, X., Zhang, Y., Shum, P., Zhang, Y., Xia, L. and Liu, D., 2012. Theoretical
407 study of dual-core photonic crystal fibers with metal wire. *IEEE photonics Journal*, 4(4),
408 pp.1178-1187.

409 [4] Chen, H.L., Li, S.G., Fan, Z.K., An, G.W., Li, J.S. and Han, Y., 2014. A novel polarization
410 splitter based on dual-core photonic crystal fiber with a liquid crystal modulation core. *IEEE*
411 *Photonics Journal*, 6(4), pp.1-9.

- 412 [5] Geng, Y., Li, X., Tan, X., Deng, Y. and Hong, X., 2013. Compact and ultrasensitive
413 temperature sensor with a fully liquid-filled photonic crystal fiber Mach-Zehnder
414 interferometer. *IEEE Sensors Journal*, 14(1), pp.167-170.
- 415 [6] Zhou, J., Wang, Y., Liao, C., Sun, B., He, J., Yin, G., Liu, S., Li, Z., Wang, G., Zhong, X.
416 and Zhao, J., 2015. Intensity modulated refractive index sensor based on optical fiber
417 Michelson interferometer. *Sensors and Actuators B: Chemical*, 208, pp.315-319.
- 418 [7] Iadicicco, A., Cusano, A., Campopiano, S., Cutolo, A. and Giordano, M., 2005. Thinned
419 fiber Bragg gratings as refractive index sensors. *IEEE Sensors Journal*, 5(6), pp.1288-1295.
- 420 [8] Patrick, H.J., Kersey, A.D. and Bucholtz, F., 1998. Analysis of the response of long period
421 fiber gratings to external index of refraction. *Journal of lightwave technology*, 16(9), p.1606.
- 422 [9] James, S.W. and Tatam, R.P., 2003. Optical fibre long-period grating sensors: characteristics
423 and application. *Measurement science and technology*, 14(5), p.R49.
- 424 [10] González-Vila, Á., Ioannou, A., Loyez, M., Debliquy, M., Lahem, D. and Caucheteur, C.,
425 2018. Surface plasmon resonance sensing in gaseous media with optical fiber gratings.
426 *Optics letters*, 43(10), pp.2308-2311.
- 427 [11] Zhou, X., Li, X., Cheng, T., Li, S. and An, G., 2018. Graphene enhanced optical fiber
428 SPR sensor for liquid concentration measurement. *Optical Fiber Technology*, 43, pp.62-66.m
- 429 [12] Liedberg, B., Nylander, C. and Lunström, I., 1983. Surface plasmon resonance for gas
430 detection and biosensing. *Sensors and actuators*, 4, pp.299-304.
- 431 [13] Dash, J.N. and Jha, R., 2014. Graphene-based birefringent photonic crystal fiber sensor
432 using surface plasmon resonance. *IEEE Photonics Technology Letters*, 26(11), pp.1092-
433 1095.
- 434 [14] Homola, J., Yee, S.S. and Gauglitz, G., 1999. Surface plasmon resonance sensors.
435 *Sensors and actuators B: Chemical*, 54(1-2), pp.3-15.
- 436 [15] Tajima, K., Zhou, J., Nakajima, K. and Sato, K., 2004. Ultralow loss and long length
437 photonic crystal fiber. *Journal of Lightwave Technology*, 22(1), p.7.
- 438 [16] Carrascosa, L.G., Sina, A.A.I., Palanisamy, R., Sepulveda, B., Otte, M.A., Rauf, S.,
439 Shiddiky, M.J. and Trau, M., 2014. Molecular inversion probe-based SPR biosensing for
440 specific, label-free and real-time detection of regional DNA methylation. *Chemical
441 communications*, 50(27), pp.3585-3588.

- 442 [17] Matsui, T., Zhou, J., Nakajima, K. and Sankawa, I., 2005. Dispersion-flattened photonic
443 crystal fiber with large effective area and low confinement loss. *Journal of Lightwave*
444 *Technology*, 23(12), pp.4178-4183.
- 445 [18] Poli, F., Cucinotta, A. and Selleri, S., 2007. *Photonic crystal fibers: properties and*
446 *applications (Vol. 102)*. Springer Science & Business Media.
- 447 [19] Rindorf, L., Jensen, J.B., Dufva, M., Pedersen, L.H., Høiby, P.E. and Bang, O., 2006.
448 Photonic crystal fiber long-period gratings for biochemical sensing. *Optics Express*, 14(18),
449 pp.8224-8231.
- 450 [20] Krohn, D.A., MacDougall, T. and Mendez, A., 2014. *Fiber optic sensors: fundamentals*
451 *and applications*. Bellingham, WA: Spie Press.
- 452 [21] Rifat, A.A., Mahdiraji, G.A., Sua, Y.M., Ahmed, R., Shee, Y.G. and Adikan, F.M., 2016.
453 Highly sensitive multi-core flat fiber surface plasmon resonance refractive index sensor.
454 *Optics express*, 24(3), pp.2485-2495.
- 455 [22] Carrascosa, L.G., Sina, A.A.I., Palanisamy, R., Sepulveda, B., Otte, M.A., Rauf, S.,
456 Shiddiky, M.J. and Trau, M., 2014. Molecular inversion probe-based SPR biosensing for
457 specific, label-free and real-time detection of regional DNA methylation. *Chemical*
458 *communications*, 50(27), pp.3585-3588.
- 459 [23] Shuai, B., Xia, L. and Liu, D., 2012. Coexistence of positive and negative refractive
460 index sensitivity in the liquid-core photonic crystal fiber based plasmonic sensor. *Optics*
461 *express*, 20(23), pp.25858-25866.
- 462 [24] Dash, J.N. and Jha, R., 2015. On the performance of graphene-based D-shaped photonic
463 crystal fibre biosensor using surface plasmon resonance. *Plasmonics*, 10(5), pp.1123-1131.
- 464 [25] Liu, C., Su, W., Liu, Q., Lu, X., Wang, F., Sun, T. and Chu, P.K., 2018. Symmetrical
465 dual D-shape photonic crystal fibers for surface plasmon resonance sensing. *Optics express*,
466 26(7), pp.9039-9049.
- 467 [26] Islam, M.S., Cordeiro, C.M., Sultana, J., Aoni, R.A., Feng, S., Ahmed, R., Dorraki, M.,
468 Dinovitser, A., Ng, B.W.H. and Abbott, D., 2019. A Hi-Bi ultra-sensitive surface plasmon
469 resonance fiber sensor. *IEEE access*, 7, pp.79085-79094.
- 470 [27] Shafkat, A., 2020. Analysis of a gold coated plasmonic sensor based on a duplex core
471 photonic crystal fiber. *Sensing and Bio-Sensing Research*, 28, p.100324.

- 472 [28] Abdullah, H., Ahmed, K. and Mitu, S.A., 2020. Ultrahigh sensitivity refractive index
473 biosensor based on gold coated nano-film photonic crystal fiber. *Results in Physics*, 17,
474 p.103151.
- 475 [29] Aoni, R.A., Ahmed, R. and Razzak, S.A., 2013, August. Design and simulation of dual-
476 concentric-core photonic crystal fiber for dispersion compensation. In *CIOMP-OSA Summer*
477 *Session on Optical Engineering, Design and Manufacturing* (p. Tu2). Optical Society of
478 America.
- 479 [30] Hu, D.J.J. and Ho, H.P., 2017. Recent advances in plasmonic photonic crystal fibers:
480 design, fabrication and applications. *Advances in Optics and Photonics*, 9(2), pp.257-314.
- 481 [31] Akowuah, E.K., Gorman, T., Ademgil, H., Haxha, S., Robinson, G.K. and Oliver, J.V.,
482 2012. Numerical analysis of a photonic crystal fiber for biosensing applications. *IEEE*
483 *Journal of Quantum Electronics*, 48(11), pp.1403-1410.
- 484 [32] Liu, C., Yang, L., Liu, Q., Wang, F., Sun, Z., Sun, T., Mu, H. and Chu, P.K., 2018.
485 Analysis of a surface plasmon resonance probe based on photonic crystal fibers for low
486 refractive index detection. *Plasmonics*, 13(3), pp.779-784.
- 487 [33] Guiyao, Z., Zhiyun, H., Shuguang, L. and Lantian, H., 2006. Fabrication of glass
488 photonic crystal fibers with a die-cast process. *Applied optics*, 45(18), pp.4433-4436.
- 489 [34] Brückner, V., 2011. To the use of Sellmeier formula. *Senior Experten Service (SES)*
490 *Bonn and HfT Leipzig, Germany*, 42, pp.242-250.
- 491 [35] Dash, J.N. and Jha, R., 2014. SPR biosensor based on polymer PCF coated with
492 conducting metal oxide. *IEEE Photonics Technology Letters*, 26(6), pp.595-598.
- 493 [36] Liu, Q., Li, S., Chen, H., Li, J. and Fan, Z., 2015. High-sensitivity plasmonic temperature
494 sensor based on photonic crystal fiber coated with nanoscale gold film. *Applied Physics*
495 *Express*, 8(4), p.046701.
- 496 [37] Rakić, A.D., Djurišić, A.B., Elazar, J.M. and Majewski, M.L., 1998. Optical properties of
497 metallic films for vertical-cavity optoelectronic devices. *Applied optics*, 37(22), pp.5271-
498 5283.
- 499 [38] Kaur, V. and Singh, S., 2019. Design of titanium nitride coated PCF-SPR sensor for
500 liquid sensing applications. *Optical Fiber Technology*, 48, pp.159-164.
- 501 [39] Monir, M.K., Hasan, M., Paul, B.K., Ahmed, K., El-Khozondar, H.J. and Amiri, I.S.,
502 2019. High birefringent, low loss and flattened dispersion asymmetric slotted core-based

503 photonic crystal fiber in THz regime. International Journal of Modern Physics B, 33(20),
504 p.1950218.

505 [40] Akowuah, E.K., Gorman, T., Ademgil, H., Haxha, S., Robinson, G.K. and Oliver, J.V.,
506 2012. Numerical analysis of a photonic crystal fiber for biosensing applications. IEEE
507 Journal of Quantum Electronics, 48(11), pp.1403-1410.

508 [41] Hautakorpi, M., Mattinen, M. and Ludvigsen, H., 2008. Surface-plasmon-resonance
509 sensor based on three-hole microstructured optical fiber. Optics express, 16(12), pp.8427-
510 8432.

511 [42] Mishra, A.K., Mishra, S.K. and Gupta, B.D., 2015. SPR based fiber optic sensor for
512 refractive index sensing with enhanced detection accuracy and figure of merit in visible
513 region. Optics Communications, 344, pp.86-91.

514 [43] C. Caucheteur, T. Guo, and J. Albert, "Review of plasmonic fiber optic biochemical
515 sensors: improving the limit of detection," Analytical and bioanalytical chemistry 407, 3883-
516 3897 (2015).

517 [44] Omar, N.A.S., Ramli, I., Fen, Y.W., Abdullah, J., Daud, N.F.M., Daniyal, W.M.E.M.M.
518 and Mahdi, M.A., 2021. A sensing approach for manganese ion detection by carbon dots
519 nanocomposite thin film-based surface plasmon resonance sensor. Optik, p.167435.

520 [45] Hashim, H.S., Fen, Y.W., Omar, N.A.S., Fauzi, N.I.M. and Daniyal, W.M.E.M.M., 2021.
521 Recent advances of priority phenolic compounds detection using phenol oxidases-based
522 electrochemical and optical sensors. Measurement, 184, p.109855.

523 [46] Paul, A.K., Sarkar, A.K., Islam, M.H. and Morshed, M., 2018. Dual core photonic crystal
524 fiber based surface plasmon resonance biosensor. Optik, 170, pp.400-408.

525 [47] Rifat, A.A., Haider, F., Ahmed, R., Mahdiraji, G.A., Adikan, F.M. and Miroshnichenko,
526 A.E., 2018. Highly sensitive selectively coated photonic crystal fiber-based plasmonic
527 sensor. Optics letters, 43(4), pp.891-894.

528 [48] Mahfuz, M.A., Hossain, M., Haque, E., Hai, N.H., Namihira, Y. and Ahmed, F., 2019. A
529 bimetallic-coated, low propagation loss, photonic crystal fiber based plasmonic refractive
530 index sensor. Sensors, 19(17), p.3794.

531 [49] Li, D., Zhang, W., Liu, H., Hu, J. and Zhou, G., 2017. High sensitivity refractive index
532 sensor based on multicoating photonic crystal fiber with surface plasmon resonance at near-
533 infrared wavelength. IEEE Photonics Journal, 9(2), pp.1-8.

- 534 [50] Ahmed, T., Paul, A.K., Anower, M.S. and Razzak, S.A., 2019. Surface plasmon
535 resonance biosensor based on hexagonal lattice dual-core photonic crystal fiber. *Applied*
536 *optics*, 58(31), pp.8416-8422.
- 537 [51] Mollah, M.A., Paul, A.K. and Razzak, S.M.A., 2018, December. Dual polarized
538 plasmonic refractive index sensor based on photonic crystal fiber. In 2018 10th International
539 conference on electrical and computer engineering (ICECE) (pp. 73-76). IEEE.
- 540 [52] Al Mahfuz, M., Mollah, M.A., Momota, M.R., Paul, A.K., Masud, A., Akter, S. and
541 Hasan, M.R., 2019. Highly sensitive photonic crystal fiber plasmonic biosensor: Design and
542 analysis. *Optical Materials*, 90, pp.315-321.